https://doi.org/10.5194/essd-2026-598
Preprint. Discussion started: 18 August 2026

Open Access Earth System Science Data Discussions

A global dataset of bias-corrected waves and storm surge (1950–2023) with improved extremes for hazard mapping

Archit Shirish Wadalkar[1], Michalis I. Vousdoukas[2], Massimo Tondello[3], Vitali Sharmar[4], Evangelos Voukouvalas[5], Salvatore Causio[4], Ivan Federico[4], Giovanni Coppini[4] and Lorenzo Mentaschi[1,4]

[1]Department of Physics and Astronomy, University of Bologna, Bologna, 40127 Bologna, Italy
[2] European Commission, Joint Research Centre (JRC), Seville, 41092, Spain
[3]HS Marine SrL, 35027 Noventa Padovana, Italy
[4]CMCC Foundation – Euro-Mediterranean Center on Climate Change, 73100 Lecce, Italy
[5]Unisystems Luxembourg Sarl, 8070 Bertrange, Luxembourg

Correspondence to: Archit Shirish Wadalkar (archit.wadalkar2@unibo.it); Lorenzo Mentaschi (lorenzo.mentaschi@unibo.it)

Abstract. Consistent global datasets of storm surges and waves are essential for assessing coastal vulnerability under changing coastal hazard conditions. Building on the global coupled hindcast, we present an enhanced hazard-oriented dataset of storm surges and bulk and spectral peak wave parameters spanning 1950–2023. Modelled significant wave heights from the hindcast are bias-corrected using satellite altimetry observations, while storm-surge signals are derived from modelled sea surface heights through frequency-based filtering. The dataset includes significant wave height, wave period, wavelength, mean wave direction, directional spreading, and spectral characteristics of the three dominant energy peaks. We validate the corrected significant wave heights against observations from 485 buoy locations and the derived storm surges against 550 tide gauges, with particular emphasis on the upper tail of the distributions. For significant wave heights, the global median normalised bias beyond the 95th percentile is −0.88 %, indicating that systematic errors in extreme wave conditions are largely removed. At higher latitudes (30° N–65° N), where tide-gauge coverage is denser, storm surges show a median normalised bias beyond the 95th percentile of 2.62 % and a median correlation of 0.81, indicating that the modelling framework captures observed storm-surge variability effectively in well-observed extratropical regions, while larger uncertainties remain in tropical and equatorial regions. Additional event-based evaluation during tropical cyclones shows limited systematic bias in modelled peak wave heights and surge levels. The resulting dataset provides a consistent global baseline for coastal hazard mapping, non-stationary extreme value analysis, regional downscaling, compound-event assessment, and data-driven modelling applications. The dataset (Wadalkar et al., 2026) is available at https://doi.org/10.2905/JRC.W0YPDCR.

1 Introduction

Coastal flooding driven by extreme sea levels (ESLs) is one of the most critical natural hazards (Wenzel et al., 2026; Koks et al., 2019; Forzieri et al., 2016) affecting global coastlines (Kirezci et al., 2025; Wang and Bernier, 2025; Jevrejeva et al., 2023). ESLs arise from the combined contribution of mean sea level, tides, storm surges, and wave-driven processes (Woodworth et al., 2021; Vousdoukas et al., 2018), and can lead to extensive inundation (Kirezci et al., 2020), shoreline erosion (Toimil et al., 2020), and damage to coastal infrastructure (Vousdoukas et al., 2020; Nawarat et al., 2026). These impacts are particularly relevant for low-lying coastal communities, ports, transport networks, and small-island or reef-fringed systems exposed to both water-level extremes and energetic waves (Nicholls et al., 2021; Storlazzi et al., 2018; Vousdoukas et al., 2023). Beyond coastal flooding, waves and storm-driven sea-level variability are also key variables for offshore engineering, navigation, climate diagnostics, and the assessment of marine extremes. Long, spatially consistent datasets of waves and storm surges are therefore needed for applications spanning coastal adaptation and risk reduction to open-ocean and offshore analyses.

Estimating the intensity and frequency of these hazards requires long, spatially consistent records of the relevant drivers. Extreme value analysis (EVA) is commonly applied to observed records to estimate return levels and characterise rare events (Watson and Lim, 2023; Wahl et al., 2017), with non-stationary approaches increasingly used to account for temporal changes in extremes (Mentaschi et al., 2016). However, global in situ observations remain unevenly distributed, with sparse coverage in many regions, frequent data gaps, and inconsistent record lengths. Numerical hindcasts help overcome these limitations by simulating the physical processes controlling waves and sea levels over multi-decadal periods, providing spatially continuous datasets suitable for regional and global hazard assessment (Muis et al., 2020; Wang and Bernier, 2025; Dong et al., 2026).

A substantial effort has therefore been dedicated to developing global wave and storm-surge hindcasts (Muis et al., 2020; Mentaschi et al., 2023; Aleksandrova et al., 2025). Coupled modelling frameworks are particularly valuable because they represent interactions between hydrodynamics and waves more consistently than approaches in which the components are simulated separately (Bakhtyar et al., 2020; Moghimi et al., 2020). Mentaschi et al. (2023) used a two-way coupled model setup to produce a global hindcast of sea surface heights and waves forced by ERA5 atmospheric reanalysis. The use of an unstructured mesh enabled coastal resolutions of approximately 2 to 4 km while maintaining global coverage and computational efficiency, leading to improved performance relative to earlier global hindcasts based on coarser grids or uncoupled configurations (Mentaschi et al., 2017; Vousdoukas et al., 2018).

Despite these advances, additional processing is needed before such hindcasts can be used as analysis-ready global datasets for ocean and coastal hazard applications. First, modelled significant wave heights may retain systematic biases, particularly in the upper tail of the distribution, partly because atmospheric reanalyses such as ERA5 can underestimate extreme wind speeds (Campos et al., 2022; Bessonova et al., 2025). Satellite altimetry provides a globally consistent observational reference for constraining wave-height distributions, and has been increasingly used to evaluate or bias-correct wave model outputs, including under extreme conditions (Ribal and Young, 2019; Dodet et al., 2020; Alday et al., 2021). Second, modelled sea surface heights must be processed to isolate storm-surge signals from low-frequency sea-level variability and high-frequency oscillations unrelated to the target storm-surge component (Barbot et al., 2024; Park et al., 2022). Third, comprehensive validation of global wave and surge products requires attention not only to standard time-series metrics but also to the representation of distributions and upper-tail behaviour. This is increasingly enabled by the expanding availability

https://doi.org/10.5194/essd-2026-598
Preprint. Discussion started: 18 August 2026

of buoy observations, GESLA3 tide-gauge records, and distribution-focused performance metrics (Haigh et al., 2023; Bessonova et al., 2025; Campos-Caba et al., 2024).

In this study, we build on the hindcast of Mentaschi et al. (2023) to produce an enhanced global dataset of storm surges and bulk and spectral peak wave parameters for 1950–2023. We apply empirical quantile mapping to bias-correct modelled significant wave heights using satellite altimetry (Liu et al., 2025), derive storm-surge signals from modelled sea surface heights through temporal filtering, and provide integrated and spectral peak wave parameters including wave height, period, wavelength, direction, and directional spreading. Preliminary validation identified a persistent residual bias in the Mediterranean Sea following the global correction, which is addressed through an additional regional refinement. The resulting dataset is distributed on the native unstructured global mesh and validated against observations from 485 buoy locations and 550 tide gauges, with emphasis on upper-tail performance and cyclone-associated extremes. It is designed to serve as a consistent global baseline for wave-climate analysis, coastal and offshore hazard mapping, regional downscaling, data-driven modelling, and non-stationary univariate or multivariate EVA of ocean extremes, including compound wave–surge events (Bahmanpour et al., 2026).

2 Materials and methods

The workflow used to generate and validate the dataset is summarised in Fig. 1. Starting from the global coupled hindcast of Mentaschi et al. (2023), two processing branches are applied. In the wave branch, modelled significant wave heights are bias-corrected using satellite altimetry through empirical quantile mapping, while the remaining bulk and spectral peak wave parameters are retained as part of the final dataset. In the sea-level branch, modelled sea surface heights are temporally filtered to isolate the storm-surge signals. The resulting fields are then validated against independent observational datasets, including buoy observations for waves and tide-gauge records for storm surges. The following subsections describe the input datasets, processing steps, validation metrics, and final data structure.

2.1 Data sources

2.1.1 Model data

We use significant wave height (Hs) and sea surface height (SSH) fields from the 73-year global SCHISM–WWM-V coupled hindcast developed by Mentaschi et al. (2023). The hindcast is based on a two-way coupled hydrodynamic and wave modelling framework implemented on an unstructured global mesh, with coastal resolution reaching approximately 2–4 km in nearshore regions. The outputs used in this study are available at 3 hourly temporal resolution. The model is forced by ERA5 reanalysis winds, sea-level pressure, and sea-ice concentration, providing continuous global coverage from 1950 onward. The Hs and SSH fields serve as the input for the wave-height bias-correction procedure and the derivation of filtered storm-surge signals, respectively.

2.1.2 Observational data

https://doi.org/10.5194/essd-2026-598
Preprint. Discussion started: 18 August 2026

Three observational datasets are used for bias correction and validation. Satellite altimetry is used as the reference dataset for bias correction of modelled significant wave heights; in situ buoy observations are used for independent validation of corrected wave heights; and tide-gauge records are used to validate the derived storm-surge signals.

For the satellite-based wave-height correction, we use the Copernicus Marine Service product "Global Ocean L3 Significant Wave Height From Reprocessed Satellite Measurements" spanning 2002–2020 (https://doi.org/10.48670/moi-00176). This product provides along-track Level-3 significant wave heights derived from multiple satellite altimetry missions, including Jason-1, Jason-2, Envisat, CryoSat-2, SARAL/AltiKa, and Jason-3. It builds on datasets developed under the ESA Sea State Climate Change Initiative and provides near-global coverage. Previous evaluations have shown good agreement with in situ buoy observations (Dodet et al., 2020; Piollé et al., 2020), supporting its use as a consistent observational reference for constraining global wave-height distributions. The relevance of satellite altimetry in extreme conditions is further supported by Tamizi and Young (2024), who compiled a dataset of altimeter observations collocated with IBTrACS (International Best Track Archive for Climate Stewardship) cyclone tracks to characterise wave conditions near tropical cyclones.

For independent validation of significant wave heights, we use in situ buoy observations. The primary source is the global compilation of Bessonova et al. (2025), which includes measurements from 444 buoy locations worldwide selected according to data availability and quality-control criteria. Buoys located in the Black Sea are excluded because the model domain does not cover this region, and one additional buoy located in the Indian Ocean (10.89° N, 72.19° E) is removed because of insufficient temporal overlap with the model output. Along the Italian coast, these observations are supplemented and updated using records from the Rete Ondametrica Nazionale (RON), maintained by the Istituto Superiore per la Protezione e la Ricerca Ambientale (ISPRA), which provide longer temporal coverage (1989–2023) and additional buoy locations. Further observations are incorporated from Sri Lanka (Luo et al., 2018) and from additional sources, including the National Data Buoy Center (NDBC), the European Marine Observation and Data Network (EMODnet), and the Copernicus Marine Environment Monitoring Service (CMEMS). Following these updates and additions, observations from 485 buoy locations with at least three months of overlap with the model period are used for validation.

For validation of storm surges, we use water-level records from the Global Extreme Sea Level Analysis dataset (GESLA3; Haigh et al., 2023). GESLA3 provides long-term hourly sea-level observations with associated quality flags, enabling the analysis of extreme water levels at tide-gauge locations worldwide. We select 550 tide gauges based on record length and data quality, following the criteria adopted in the SurgeMIP framework (Wang and Bernier, 2025; Bernier et al., 2024). These water-level records are processed to derive storm-surge residuals as described in Sect. 2.2.

https://doi.org/10.5194/essd-2026-598
Preprint. Discussion started: 18 August 2026

Open Access Earth System Science Data Discussions

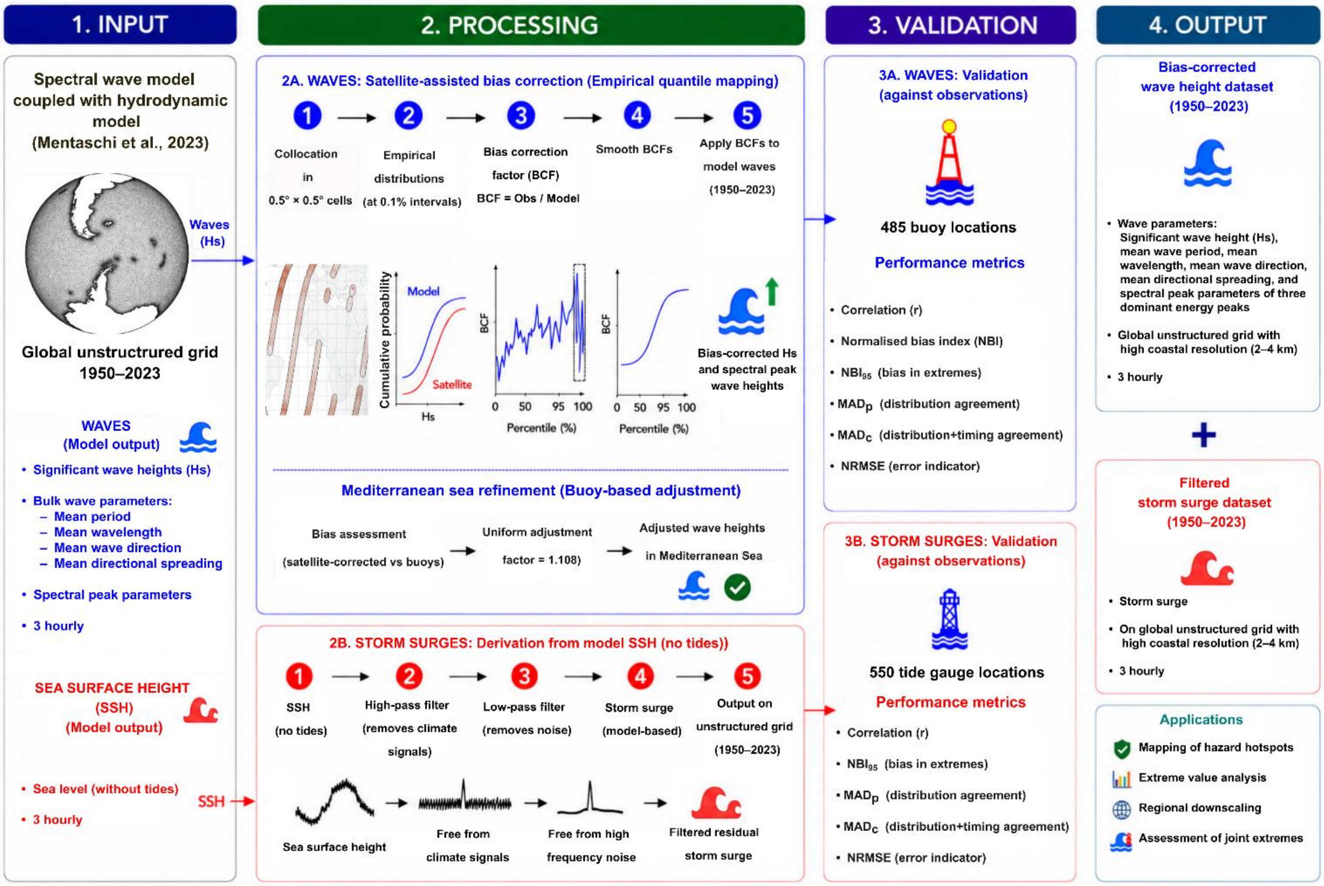

Figure 1: Schematic workflow for generating and validating the enhanced global wave and storm-surge dataset. Starting from the coupled hindcast of Mentaschi et al. (2023), modelled significant wave heights are bias-corrected using satellite altimetry through empirical quantile mapping, while storm-surge signals are derived from modelled sea surface heights through temporal filtering. The corrected wave-height fields and derived storm surges are validated against in situ buoy and tide-gauge observations, respectively. The final 3 hourly dataset spans 1950–2023 and is distributed on the native unstructured mesh together with bulk and spectral peak wave parameters.

2.2 Data processing and bias correction

2.2.1 Bias correction of wave heights

Bias correction of model-derived significant wave heights (Hs) is performed using an empirical quantile mapping approach in which model-derived Hs values are compared to satellite altimetry observations. The global ocean is divided into 0.5° × 0.5° grid cells, within which model-derived and satellite-derived Hs values are collocated along available satellite tracks over

https://doi.org/10.5194/essd-2026-598
Preprint. Discussion started: 18 August 2026

coincident time periods. Percentiles are computed from the empirical distributions of the modelled and observed values at 0.1 % intervals over the percentile range 0.1–100 %. For each percentile p within a grid cell c, a bias correction factor (BCF) is defined as the ratio of observed to modelled values.

$$BCF\ (p,c) = \frac{Hs_{obs}\ (p,c)}{Hs_{model}\ (p,c)} \tag{1}$$

where $Hs_{obs}\ (p,c)$ and $Hs_{model}\ (p,c)$ denote the observed and modelled significant wave heights at percentile p within grid cell c, respectively.

The resulting BCFs are used to adjust the model-derived wave heights. Corrections are primarily applied to higher percentiles. For percentiles below the 50th percentile, a single correction factor, equal to the BCF estimated at the lower boundary of the corrected range, is applied uniformly, ensuring continuity across the transition and avoiding artificial discontinuities in the corrected distribution. This approach is motivated by previous findings that model biases are generally small for lower wave heights but increase substantially toward the upper tail of the distribution (Mentaschi et al., 2023). This behaviour is also evident in the comparison with buoy observations shown in Supplementary Fig. S1, where the original hindcast reproduces low and moderate wave heights reasonably well, while deviations increase progressively toward the upper tail of the distribution. Given that the primary objective of this dataset is to support the analysis of extreme events, emphasis is placed on improving the representation of extreme wave conditions.

To reduce sampling noise and ensure a stable representation of the upper tail, BCF values at higher percentiles are smoothed using a fifth-order polynomial fit. This provides sufficient flexibility to capture nonlinear behaviour in extreme values while avoiding overfitting. Additional constraints are applied to ensure a smooth transition between corrected and uncorrected percentiles and to limit unrealistic amplification at the highest percentiles. Tests using alternative smoothing approaches, including Savitzky–Golay filtering, yielded comparable results, indicating that the correction is not sensitive to the specific smoothing method.

The bias-corrected wave heights are obtained by multiplying the modelled percentile values by the corresponding smoothed BCFs. The derived correction factors are assumed to be stationary within each grid cell and are applied uniformly across the hindcast period (1950–2023). This procedure is applied within the latitude range 66° S–70° N. Regions outside this range are excluded due to the presence of sea ice and the scarcity of reliable altimetric observations. The significant wave heights associated with the partitioned spectral peaks are corrected using the same factors as those used for the total Hs, ensuring consistency among the wave-height variables.

2.2.2 Filtering the storm-surge signal

The storm-surge signals are derived from sea surface height (SSH) time series for both the model output and observational datasets. For the model data (Mentaschi et al., 2023), SSH is available at a temporal resolution of 3 hours, with tidal forcing

https://doi.org/10.5194/essd-2026-598
Preprint. Discussion started: 18 August 2026

excluded from the simulations. Therefore, the model output represents non-tidal residual water levels, and no detiding procedure is required. To isolate the storm surge component, the time series is filtered to remove both low-frequency variability associated with long-term sea-level changes and high-frequency noise. This is achieved using a combination of high-pass and low-pass Butterworth filters following the methodology of Campos-Caba et al. (2024) and Park et al. (2022). A second-order high-pass Butterworth filter with a cutoff period of 60 days is applied to remove low-frequency climatic signals. A second-order low-pass Butterworth filter with a cutoff period of 12 hours is applied to remove high-frequency oscillations unrelated to storm-surge dynamics.

For the observational data from GESLA3, which are provided at hourly temporal resolution and include tidal contributions, storm surge residuals are derived. The mean sea level is first removed from the time series. The tidal component is then estimated and removed using the pytides Python module, which performs harmonic analysis based on 37 tidal constituents including K_1, O_1, M_2, and S_2, using one-year segments of data. The resulting non-tidal residuals are subsequently filtered using the same combination of high-pass and low-pass filters as applied to the model data. Before comparison, the processed GESLA3 time series are aggregated to a temporal resolution of 3 hours by averaging consecutive hourly values.

2.2.3 Regional adjustment in the Mediterranean Sea

During validation of the bias-corrected model-derived significant wave heights (Hs) against in situ buoy observations, a persistent negative bias of approximately 5 % was identified in the Mediterranean Sea. This discrepancy might be associated with differences between satellite-derived wave heights and buoy measurements in semi-enclosed basins. To account for this regional bias, an additional uniform adjustment factor of 1.108 is applied to the corrected Hs values within the Mediterranean Sea. The adjustment factor is derived directly from the observed regional median bias relative to buoy observations. This regional adjustment improves the representation of extreme wave conditions, which are critical for coastal hazard assessments and the estimation of return levels in the Mediterranean region. The impact of the satellite-based correction and subsequent Mediterranean refinement on both local and basin-scale performance is illustrated in Supplementary Fig. S1.

2.3 Performance metrics used for validation

The dataset is evaluated using a suite of statistical metrics with emphasis on the representation of extreme conditions relevant to coastal hazard assessments. Since significant wave height (Hs) is strictly positive whereas storm surges can take both positive and negative values, slightly different formulations are adopted for the two variables.

2.3.1 Performance metrics for waves

Standard statistical metrics include the Pearson correlation coefficient (r), normalised bias index (NBI), and normalised root mean squared error (NRMSE). The Pearson correlation coefficient is defined as

https://doi.org/10.5194/essd-2026-598
Preprint. Discussion started: 18 August 2026

Open Access Earth System Science Data Discussions

$$r = \frac{1}{N-1}\sum_{i=1}^{N}\left(\frac{M_i - \mu_M}{\sigma_M}\right)\left(\frac{O_i - \mu_O}{\sigma_O}\right) \tag{2}$$

where M_i and O_i denote the modelled values from the dataset and observed values at common time step i, respectively; μ_M and μ_O represent their mean values; σ_M and σ_O their standard deviations; N is the sample size.

The normalised bias index is defined as

$$NBI = \frac{\sum_{i=1}^{N}(M_i - O_i)}{\sum_{i=1}^{N} O_i} \times 100\ \% \tag{3}$$

and the normalised root mean squared error (NRMSE) is defined as

$$NRMSE = \sqrt{\frac{\sum_{i=1}^{N}(M_i - O_i)^2}{\sum_{i=1}^{N}(O_i)^2}} \tag{4}$$

To assess the performance of waves under extreme conditions, normalised bias is also computed for values exceeding the 95th percentile of observations (NBI_{95}), defined as

$$NBI_{95} = \frac{\overline{M_{95}} - \overline{O_{95}}}{\overline{O_{95}}} \times 100\ \% \tag{5}$$

where $\overline{M_{95}}$ and $\overline{O_{95}}$ denote the average of values exceeding the 95th percentile in bias-corrected wave heights from the dataset and observed distributions, respectively. Additional metrics based on the 99th percentile are provided in Supplementary Fig. S3.

Further, the slope (m) and intercept (b) of the linear regression between the values in the dataset and observed values are computed as

$$M = mO + b \tag{6}$$

To evaluate the agreement between the dataset derived from the model and the observed distributions, percentile-based metrics are adopted following Campos-Caba et al. (2024). The mean absolute deviation of percentiles (MAD_p) and the corrected mean absolute deviation (MAD_c) are defined as

$$MAD_p = \overline{|M_{prc} - O_{prc}|} \tag{7}$$

$$MAD_c = MAD_p + \overline{|M - O|} \tag{8}$$

https://doi.org/10.5194/essd-2026-598
Preprint. Discussion started: 18 August 2026

Percentiles from 0 % to 100 %, after every 1 % are represented by M_{prc} and O_{prc}. The additional term in MAD_c accounts for timing mismatches between peaks of values from the dataset and those from observations, thereby penalising situations where the magnitude of extremes is reproduced but their temporal occurrence is displaced.

For comparison with the satellite product, model outputs are aggregated to 0.5° × 0.5° grid cells and metrics are computed using coincident observations during the period 2002–2020.

2.3.2 Performance metrics for storm surges

For storm surges, correlation and error-based metrics are used. The standard normalised bias is not considered because storm surges can take both positive and negative values; however, a percentile-based bias metric is computed for the upper tail of the distribution.

The normalised RMSE is defined relative to the observed range,

$$NRMSE = \frac{\sqrt{\frac{\sum_{i=1}^{N}(M_i - O_i)^2}{N}}}{O_{99} - O_1} \tag{9}$$

where O_{99} and O_1 denote the 99th and first percentiles of the observed storm surge series, respectively. Thus, the RMSE is normalised using the observed dynamic range at each location.

Similarly, the normalised bias beyond the 95th percentile is computed using exceedances above the respective percentile thresholds of model- and observation-based distributions and normalised by the observed dynamic range.

$$NBI_{95} = \frac{\overline{M_{95}} - \overline{O_{95}}}{(O_{99} - O_1)} \times 100\ \% \tag{10}$$

where $\overline{M_{95}}$ and $\overline{O_{95}}$ denote the average of values exceeding the 95th percentile in model-derived storm surges and observed distributions, respectively. Supplementary Fig. S4 presents analogous metrics computed for exceedances above the 99th percentile. The remaining metrics are computed following the same definitions as for wave heights. These metrics are estimated using the processed 3 hourly GESLA3 storm-surge time series described in Sect. 2.2.2.

Values approaching unity indicate better performance for correlation and regression slope, whereas values approaching zero indicate lower errors for the remaining metrics.

2.3.3 Performance metrics for peaks during tropical cyclone events

To evaluate model performance under tropical cyclone conditions, event-based peak metrics are computed using IBTrACS-based cyclone tracks from the dataset provided by Tamizi and Young (2024). For each cyclone event, observational data are searched within the radius of gale-force winds (R34). If no observations are available within R34 , the search radius is expanded to 1.2 times R34 , and subsequently to a maximum distance of 100 km from the cyclone track.

For each matched cyclone event, the maximum observed and modelled values during the storm time window are extracted and compared. Two metrics used, the peak bias (PB) and absolute peak difference (APD), are respectively defined as:

$$PB = \mathrm{M}_{peak} - \mathrm{O}_{peak} \tag{11}$$

$$APD = |\mathrm{M}_{peak} - \mathrm{O}_{peak}| \tag{12}$$

where M_{peak} and O_{peak} are peak values from the present dataset and observations during the event, respectively. These metrics provide a direct assessment of the ability of the model-based dataset to reproduce cyclone-associated extremes. The event-based approach is adopted because cyclone hazards are primarily governed by peak conditions rather than long-term statistics.

2.4 Dataset description

The final dataset is distributed in NetCDF format on the native unstructured mesh from Mentaschi et al. (2023) and is provided as daily files covering the period 1950–2023. Each file contains the spatial coordinates of the computational nodes together with sea surface height, significant wave height, and a suite of integrated wave parameters and spectral peak characteristics derived from the spectral wave model**.** The dataset is stored as daily NetCDF files, each containing all 3 hourly values for the corresponding day with names ending in the format: "_YYYYMMDD.nc" where YYYYMMDD denotes the corresponding date. These variables support applications ranging from hazard assessment to wave climate studies and regional downscaling. Table 1 summarises the variables included in the released dataset.

Variable name in NetCDF	Description	Unit
x	Node longitude	° E
y	Node latitude	° N
SSH	Storm surge	m
SWH	Significant wave height	m
T01	Mean period weighted on the spectral component energy	s
T02	Zero-crossing mean period	s
T10	Mean period for overtopping/runup	s

https://doi.org/10.5194/essd-2026-598
Preprint. Discussion started: 18 August 2026

MWL	Mean wavelength	m
MWD	Mean wave direction, oceanographic convention	°N
MDS	Mean directional spreading	°
SIC	Surface ice concentration, given as ratio of ice on total surface (from ERA5)	dimensionless
SWHP1	Significant wave height of the largest spectral peak	m
T01P1	Mean period of the largest spectral peak	s
MWDP1	Mean direction of the largest spectral peak	° N
MDSP1	Directional spread of the largest spectral peak	°
SWHP2	Significant wave height of the second-largest spectral peak	m
T01P2	Mean period of the second-largest spectral peak	s
MWDP2	Mean direction of the second-largest spectral peak	° N
MDSP2	Directional spread of the second-largest spectral peak	°
SWHP3	Significant wave height of the third-largest spectral peak	m
T01P3	Mean period of the third-largest spectral peak	s
MWDP3	Mean direction of the third-largest spectral peak	° N
MDSP3	Directional spread of the third-largest spectral peak	°

Table 1. Variables included in the released NetCDF dataset, together with their NetCDF variable names, descriptions, and units.

3 Validation of the dataset

3.1 Comparison with the Copernicus Marine Service satellite product

The performance of the bias-corrected model-derived significant wave heights relative to the Copernicus Marine Service satellite product is shown in Fig. 2 using the metrics defined in Sect. 2.3. The global median NBI is 0.09 %, indicating that systematic bias in the central tendency of the wave-height distribution has been largely removed. Residual negative biases are mainly confined to high-latitude regions, where correction is not applied because of sea-ice contamination and associated uncertainties in satellite observations. It should be noted that the bias-correction procedure is applied only within the latitude range 66° S–70° N.

The median NBI_{95} is 2.67 %, indicating a modest positive bias in the upper tail of the distribution. This behaviour is spatially diffuse and may partly reflect the smoothing applied to the bias-correction factors at high percentiles. The distribution-based metrics yield global median values of 0.29 m for MAD_p and 0.63 m for MAD_c. Larger errors occur primarily in the Southern Ocean, where both model and observational uncertainties are greater.

Overall, the comparison indicates that the bias-correction procedure substantially reduces systematic errors while preserving the spatial structure of extreme wave conditions.

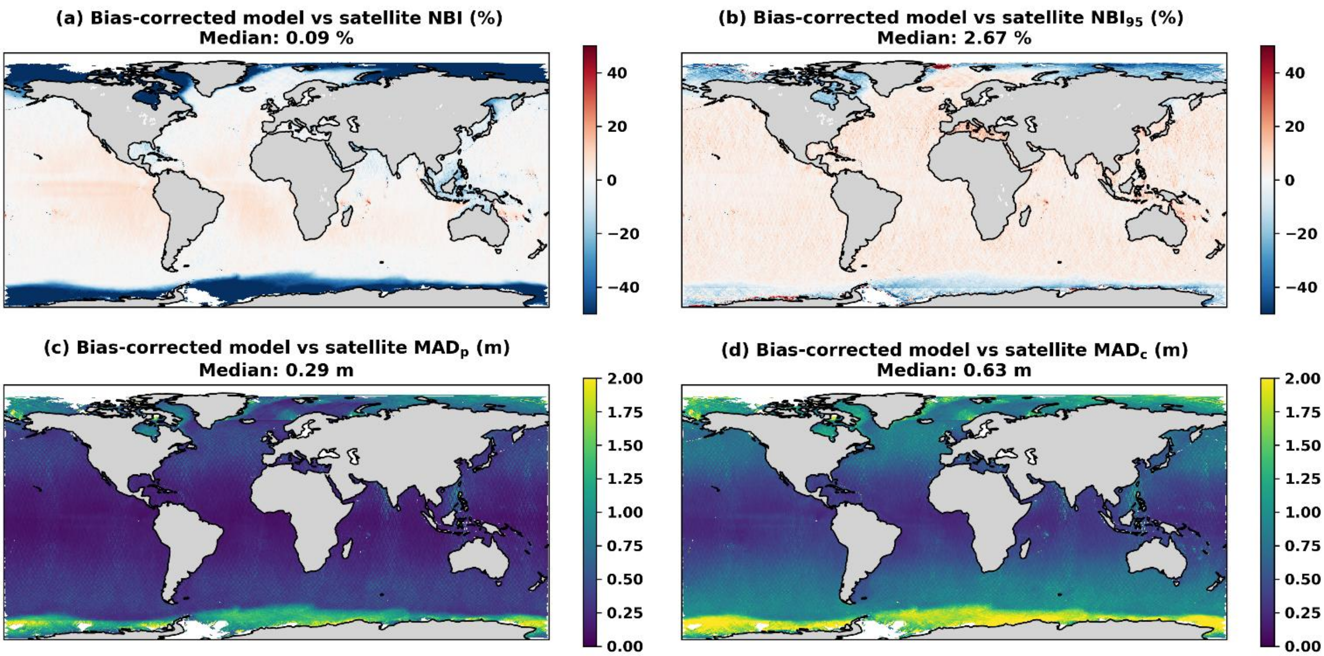

Figure 2: Global comparison of bias-corrected significant wave height (Hs) from the present dataset with Copernicus Marine Service Level-3 wave heights. Panels show (a) normalised bias (NBI, %), (b) normalised bias beyond the 95th percentile (NBI_{95}, %), (c) mean absolute deviation of percentiles (MAD_p, m), and (d) corrected mean absolute deviation (MAD_c, m). Median values are shown for each metric.

3.2 Comparison with the in situ buoys

An independent validation of the bias-corrected wave heights from the present dataset against 485 in situ buoy observations is shown in Fig. 3. At the median (Fig. 3a), the normalised bias (NBI) is 1.27 %, reflecting a limited residual bias relative to buoy observations. At higher percentiles (Fig. 3b), the median normalised bias beyond the 95th percentile (NBI_{95}) is −0.88 %. A Wilcoxon signed-rank test applied to the per-buoy median biases (n = 485) yields $p = 0.07$. Thus, the null hypothesis of zero

https://doi.org/10.5194/essd-2026-598
Preprint. Discussion started: 18 August 2026

median bias cannot be rejected at the 5 % significance level, indicating that the observed median residual bias cannot be distinguished statistically from zero. This, together with the small magnitude of the bias, suggests that systematic errors in the upper tail of the wave-height distribution have been largely removed by the bias-correction procedure. At most of the buoy locations, the NBI and NBI_{95} values are close to zero, although localised positive biases remain in parts of East Asia and Australia.

The distribution-based error metrics remain low across most locations, with median MAD_p and MAD_c values of 0.10 m and 0.40 m, respectively (Fig. 3c–d). MAD_p values are below 0.2 m at approximately 82 % of buoy locations. The median correlation across all buoy locations is 0.91, and correlations are greater than 0.9 at approximately 61 % of buoy locations. Together with the low MAD_p and MAD_c values, these results demonstrate that the dataset reproduces both the distribution and temporal variability of significant wave heights across a wide range of oceanographic conditions.

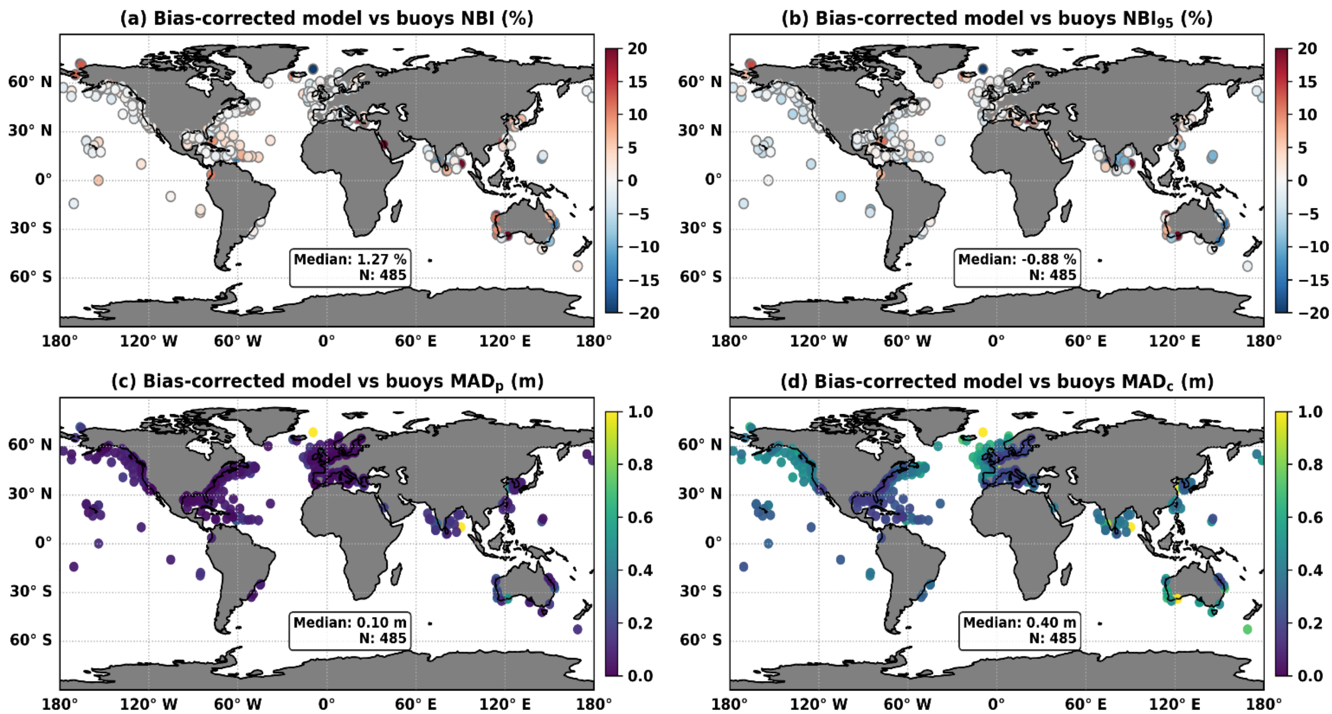

Figure 3: Global comparison of bias-corrected significant wave heights from the present dataset (Hs) against in situ buoy observations. (a) Normalised bias (NBI, %), (b) normalised bias beyond the 95th percentile (NBI_{95}, %), (c) mean absolute deviation of percentiles (MAD_p, m), and (d) corrected mean absolute deviation (MAD_c, m). Median values are indicated for each metric.

Regional median performance metrics are summarised in Table 2. Regions were defined to group buoy locations into geographically coherent ocean basins or coastal sectors with sufficient observational coverage to permit robust regional statistics. The regional groupings used for this analysis are shown in Supplementary Fig. S2. Wave heights in the present

https://doi.org/10.5194/essd-2026-598
Preprint. Discussion started: 18 August 2026

dataset exhibit close correspondence in the Mediterranean Sea, North Atlantic–European sector, and along the eastern coast of North America, whereas broader density distributions are visible at several locations in East Asia and Australia (Fig. 3; Table 2; Fig. 4). In Mediterranean Sea, the wave heights from the present dataset have a median correlation of 0.93 across the buoy locations, median NBI effectively equal to zero, and median MAD_p of 0.09 m following the regional adjustment described in Sect. 2.2.3. The regional median MAD_c value is lowest in the Mediterranean Sea (0.27 m), suggesting that the refinement improves both the distribution and timing consistency relative to buoy observations. The correlations between the dataset and observed wave heights at some locations are very close to unity, for example 0.96 at Ragusa (Fig. 4k). The improvement achieved through the satellite-based correction and subsequent Mediterranean refinement is illustrated in Supplementary Fig. S1. Similarly, across North European buoy locations, the dataset shows strong performance, with a median correlation of 0.93, median NBI of 0.53 %, and median MAD_p of 0.09 m. In both regions, median NBI and NBI_{95} values are not statistically distinguishable from zero according to the Wilcoxon signed-rank test ($p > 0.05$).

The largest positive residual biases occur near the Korean Peninsula and along the western Australian coastline. For Korea–East Asia region, median NBI and NBI_{95} values are 9.7 % and 5.01 %, respectively. And, a median NBI_{95} value of 9.66 % is obtained in the Western Australian region. These regional patterns are consistent with findings reported by Bessonova et al. (2025), who identified positive biases in ERA5-based wave products in parts of the western Pacific and southern Indian Ocean. Such discrepancies may be associated with uncertainties in atmospheric forcing, unresolved regional coastal processes, and the potential presence of bias in the satellite reference product.

Region	Number of buoys (N)	r	NBI (%)	NBI_{95} (%)	MAD_p (m)	MAD_c (m)
Mediterranean Sea	41	0.93	–0.00[a]	3.15[a]	0.09	0.27
North Europe	101	0.93	0.53[a]	0.87[a]	0.09	0.47
East North America	145	0.92	0.67	–1.59	0.09	0.29
West North America	93	0.90	1.66	–2.67	0.10	0.45
North Indian Ocean	19	0.89	–0.67[a]	–3.58[a]	0.16	0.39
Korea–East Asia	32	0.90	9.75	5.01	0.13	0.42
West Australia	14	0.88	12.44	9.66	0.30	0.67
East Australia	11	0.86	1.81[a]	–1.55[a]	0.15	0.53
All	485	0.91	1.27	–0.88[a]	0.10	0.40

[a] The corresponding median bias is not statistically distinguishable from zero according to the Wilcoxon signed-rank test ($p > 0.05$).

https://doi.org/10.5194/essd-2026-598
Preprint. Discussion started: 18 August 2026

Table 2. Regional median performance metrics for bias-corrected significant wave heights in the present dataset relative to buoy observations. Metrics include Pearson correlation coefficient (r), normalised bias (NBI), normalised bias beyond the 95th percentile (NBI_{95}), mean absolute deviation of percentiles (MAD_p), and corrected mean absolute deviation (MAD_c). *N* denotes the number of buoy locations within each region.

Figure 4 presents scatter density comparisons between significant wave heights from the present dataset and those from buoy observations at 16 representative buoy locations. The fitted slopes are generally close to unity, and the highest densities remain concentrated around the 1:1 line, showing consistent reproduction of both the magnitude and variability of wave conditions. Overall, the buoy validation demonstrates that the bias-corrected dataset reproduces significant wave heights skilfully at the global scale, with localised uncertainties.

https://doi.org/10.5194/essd-2026-598
Preprint. Discussion started: 18 August 2026

Open Access Earth System Science Data Discussions

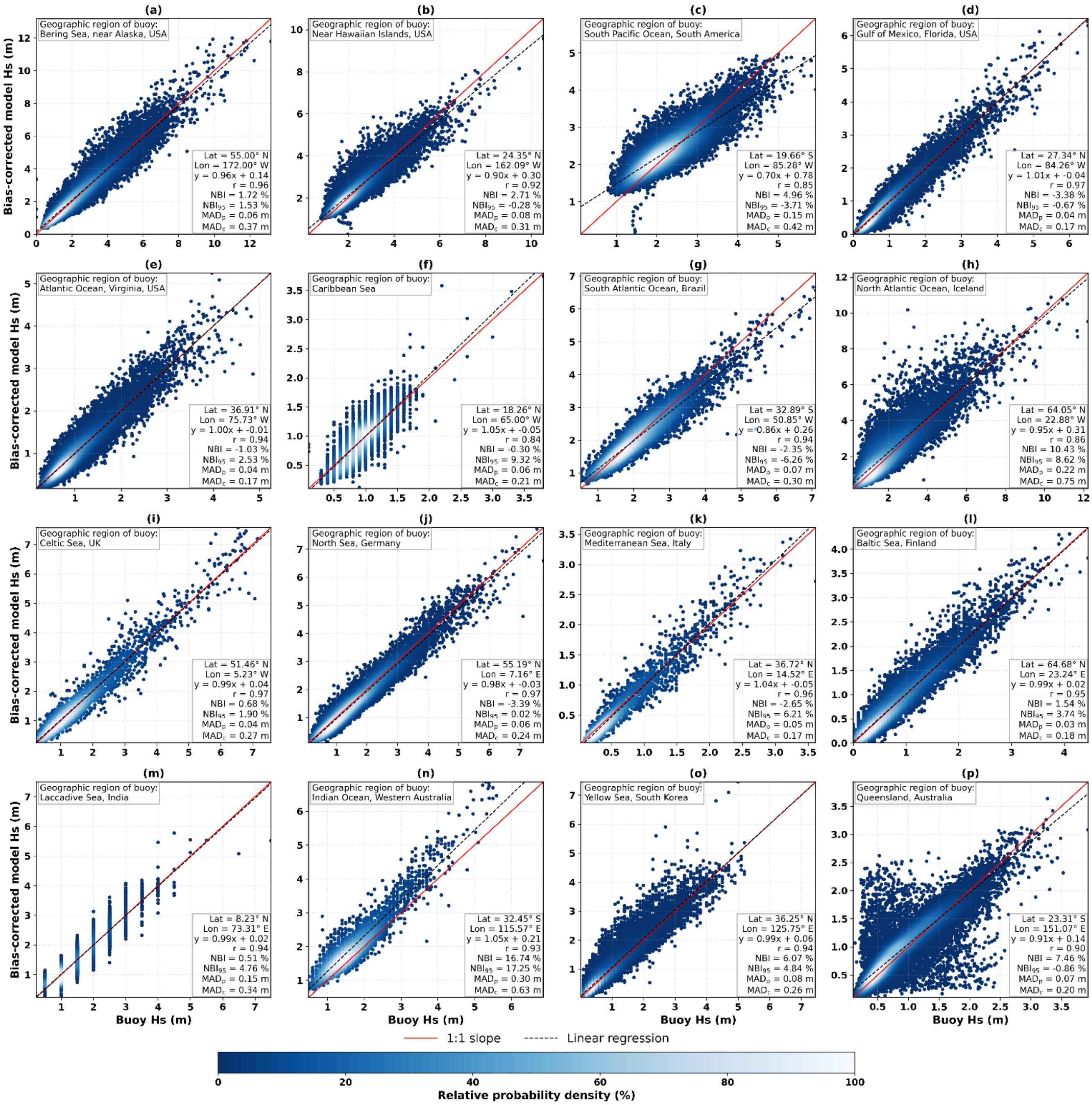

Figure 4: Scatter density plots comparing bias-corrected significant wave heights from the present dataset (Hs) with buoy observations at 16 representative locations, showing a 1:1 reference line, regression fit, and associated performance metrics.

https://doi.org/10.5194/essd-2026-598
Preprint. Discussion started: 18 August 2026

Open Access Earth System Science Data Discussions

Key performance metrics, including normalised bias index (NBI), normalised bias beyond 95th percentile (NBI_{95}), mean absolute deviation of percentiles (MAD_p), and corrected mean absolute deviation (MAD_c), are indicated for each location.

3.3 Comparison of model-derived storm surges with GESLA3 tide gauge observations

The performance of model-derived storm surges relative to storm-surge residuals derived from the selected GESLA3 tide gauges is shown in Fig. 5. The upper panels present the correlation coefficient and normalised bias beyond the 95th percentile (NBI_{95}), while the lower panels show the distribution-based error metrics MAD_p and MAD_c. The median correlation across all 550 tide gauge locations is approximately 0.72. Similar to the source sea surface heights reported by Mentaschi et al. (2023), validation performance of the storm surges in the present dataset varies with both latitude and ocean basin. Correlations are generally higher, often exceeding 0.7, at mid- and high-latitudes, while lower values, frequently below 0.5, occur more often in tropical and equatorial regions. The median NBI_{95} is approximately 0.84 % and is not statistically distinguishable from zero according to the Wilcoxon signed-rank test (p-value is close to 0.5 >> 0.05), although substantial regional positive and negative deviations remain evident. The median MAD_p and MAD_c values are 0.014 m and 0.062 m, respectively, indicating that surge distributions are reproduced within a few centimetres at most locations.

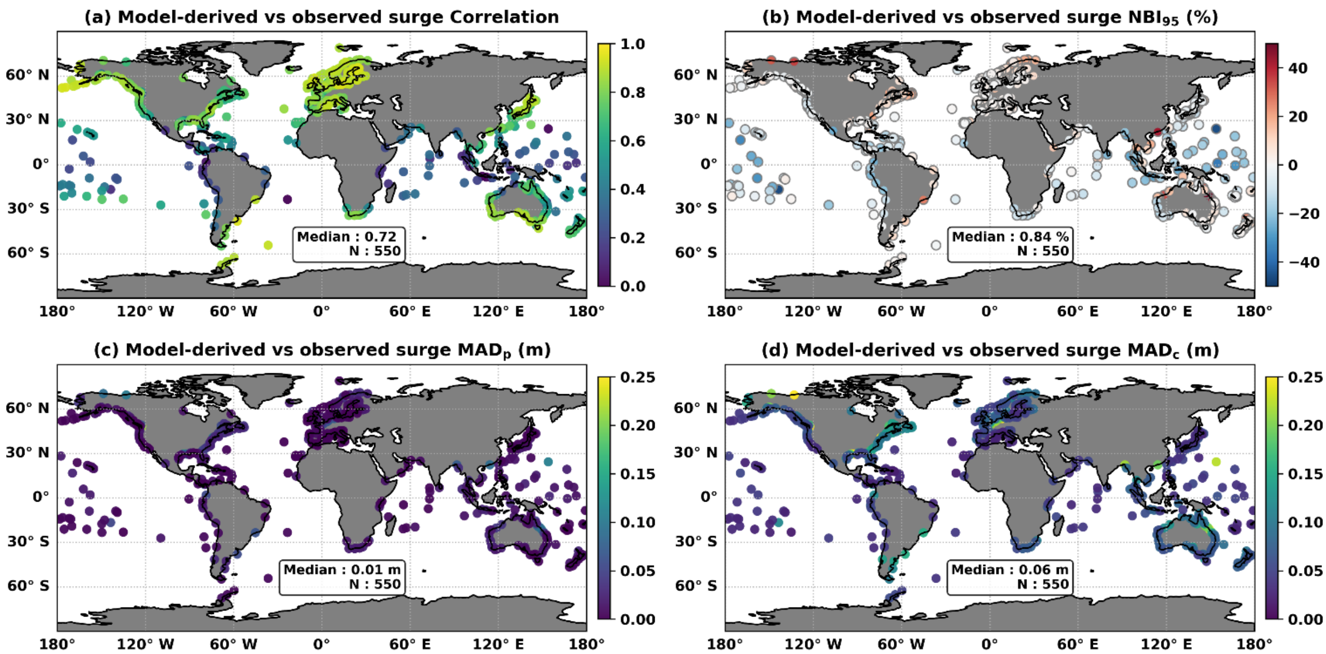

Figure 5: Global comparison of model-derived storm surges from the present dataset with storm-surge residuals derived from GESLA3 observations at 550 tide gauge locations. Panels show (a) the Pearson correlation coefficient, (b) normalised bias beyond the 95th percentile (NBI_{95}, %), (c) mean absolute deviation of percentiles (MAD_p, m), and (d) corrected mean absolute deviation (MAD_c, m). Median values are indicated for each metric.

https://doi.org/10.5194/essd-2026-598
Preprint. Discussion started: 18 August 2026

The spatial distribution of the performance metrics reveals a clear dependence on latitude, ocean basin, and coastal setting. The modelled surge shows a high association with observed surges along the North European coast, including the North Sea, Baltic Sea, and northeastern Atlantic Ocean, as well as in the Mediterranean Sea. High correlations are also observed along high-latitude North Pacific coasts, including Alaska and northern Japan (45° N–60° N), and along parts of the Tasman Sea and New Zealand coast (Fig. 5; Fig. 6). In these regions, correlation values commonly exceed 0.8, while MAD_p and MAD_c remain close to or below their global median values. Model performance against Mediterranean and North European tide-gauge observations is characterised by median correlations of 0.83 and 0.86, with corresponding MAD_p values of 0.004 m and 0.018 m and MAD_c values of 0.031 m and 0.081 m, respectively. In the Northern Hemisphere (30° N–65° N), the model-derived surges show a median correlation of 0.81 and median NBI_{95} of 2.62 % relative to observed surges derived from 290 tide gauge locations, while the median of MAD_p and MAD_c there are very close to that of the global median.

At several mid-latitude tide gauge locations along the Atlantic coasts of South and North America, NBI_{95} values exceed 10 %, and MAD_c values are greater than the global median of 0.062 m. Performance metrics of the storm surges in the dataset generally improve from mid to high latitudes along both sides of the North Pacific basin, as similar metrics are obtained at tide-gauge locations near Alaska and northern Japan. Likewise, the performance metrics along the South African coast closely resemble those obtained along the western Australian coast at comparable latitudes on the opposite side of the South Indian Ocean.

In tropical and equatorial regions (30° S–30° N), correlations are generally lower (< 0.5), and NBI_{95} values are predominantly negative, for example in the equatorial Pacific Ocean where biases approach −20 % at several tide gauge locations. However, basin-dependent exceptions exist. Positive NBI_{95} values are estimated at several locations in the South China Sea and moderate correlations, as reflected by the Vietnam station shown in Fig. 6. The lower skill observed in many tropical regions may reflect the reduced short-term variability of sea levels at low latitudes, the limited contribution of rare tropical cyclone events to the overall signal, uncertainties in ERA5 forcing during extreme events, and limitations of a depth-averaged barotropic framework in representing equatorial circulation processes and associated low-frequency variability (Mentaschi et al., 2023). In this region (30° S–30° N), the model-derived surges show median correlation below 0.4 and median NBI_{95} of −6.62 % relative to observed surges derived from 193 tide gauge locations. However, the median of MAD_p is 0.012 m, which is slightly lower than the global median across 550 gauges, and the median MAD_c is 0.047 m, which is significantly lower than the global median. Hence, despite relatively weak correlations and substantial normalised negative bias, the absolute errors in distribution and overall are lower than those of regions that are densely observed, because of the low amplitude of the surge signal in this region. Lastly, in the Southern Hemisphere (65° S–30° S), the median correlation is approximately 0.75, and NBI_{95} has a median of 1.00 % across the 52 tide gauge locations. The median MAD_p and MAD_c here are slightly worse than the global median; however, these estimates are limited by the sparse observations.

Figure 6 presents scatter-density comparisons between modelled and observed storm surges at 16 representative tide gauge locations. These patterns are consistent with the spatial distribution of the performance metrics shown in Fig. 5.

https://doi.org/10.5194/essd-2026-598
Preprint. Discussion started: 18 August 2026

Open Access Earth System Science Data Discussions

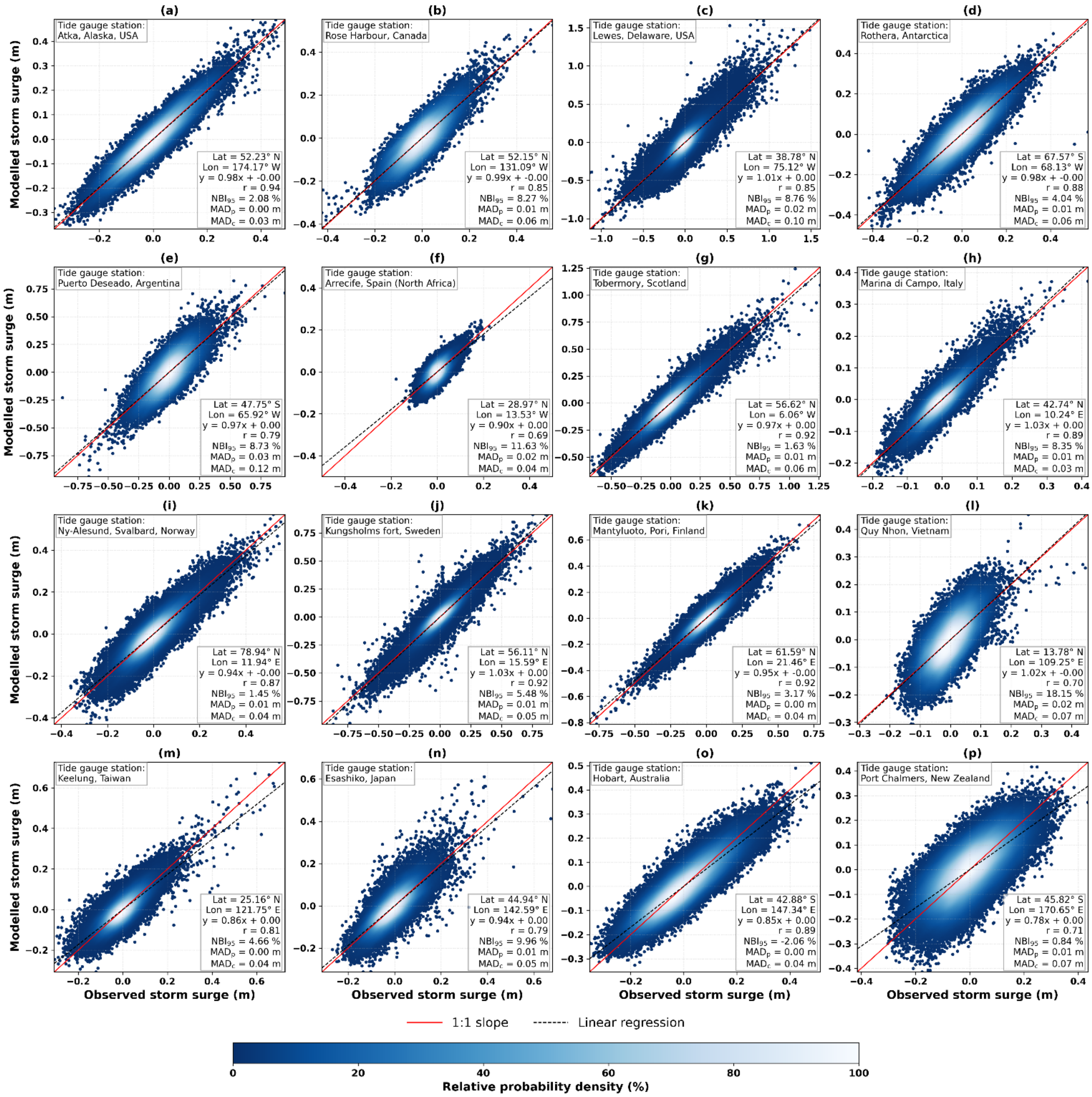

Figure 6: Scatter density plots comparing model-derived storm surges from the present dataset with storm-surge residuals derived from GESLA3 tide gauge observations at 16 representative coastal locations. Each panel shows observed versus modelled surge levels, with the 1:1 reference line. Key performance metrics, including correlation coefficient (r), normalised

https://doi.org/10.5194/essd-2026-598
Preprint. Discussion started: 18 August 2026

bias beyond 95th percentile (NBI_{95}), mean absolute deviation of percentiles (MAD_p), and corrected mean absolute deviation (MAD_c), are reported for each location.

3.4 Data evaluation during tropical cyclone events

An additional evaluation of the dataset is performed for tropical cyclone conditions using IBTrACS-based cyclone tracks from Tamizi and Young (2024). Figure 7 shows representative comparisons between modelled and observed wave heights and storm surges during cyclone events across multiple ocean basins.

To evaluate performance more systematically, peak metrics are computed for all matched cyclone events. A total of 944 matched cyclonic wave cases are extracted from the 3264 available storm-track files, 2927 of which represent tropical cyclones. The median signed peak bias is −0.25 m, and the median absolute peak error is 0.60 m, across the obtained 944 cases. For storm surges, 3275 cyclone-event cases are identified across 550 tide gauges, yielding a median signed peak bias of −0.03 m and a median absolute peak error of 0.06 m. These results indicate that the dataset reproduces cyclone-associated wave and surge extremes with limited systematic bias at the global scale.

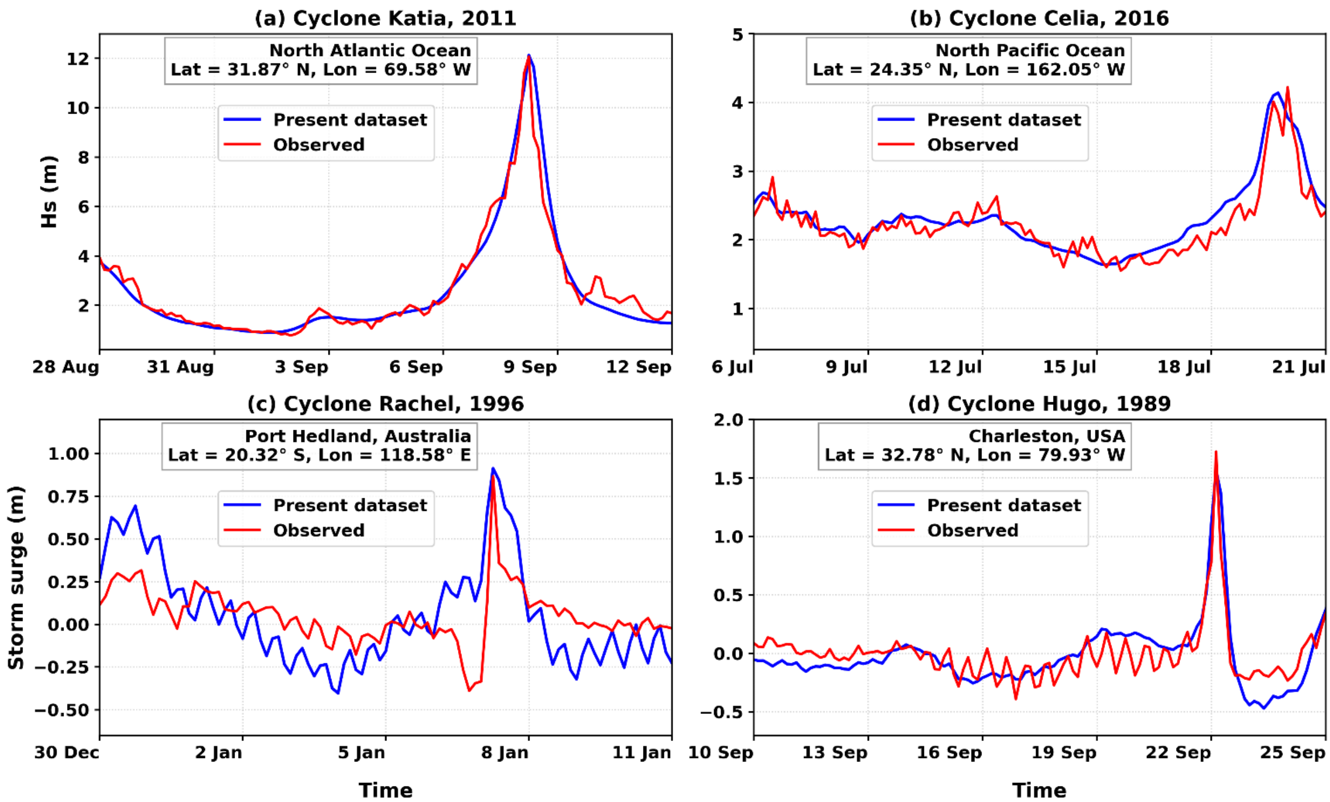

Figure 7: Comparison between the present dataset and observations during representative tropical-cyclone events in several ocean basins. Panels (a–b) show significant wave heights (Hs) during Cyclones Katia (2011) and Celia (2016), while panels

https://doi.org/10.5194/essd-2026-598
Preprint. Discussion started: 18 August 2026

(c–d) show storm surges during Cyclones Rachel (1996) and Hugo (1989). Blue lines represent the present dataset, and red lines represent observations.

For example, during Cyclone Katia (2011), peak significant wave heights reaching as high as 12 m are captured accurately (Fig. 7). Similar correspondence between observed and modelled wave evolution is evident during Cyclone Celia (2016) in the North Pacific. For storm surges, the Port Hedland record associated with Cyclone Rachel (1996) exhibits oscillatory behaviour characteristic of cyclone-induced coastal seiches, which is reproduced by the model, as this tide gauge station is situated close to the open coast. Likewise, the surge peak and subsequent recession associated with Cyclone Hugo (1989) are represented consistently.

4 Discussion and perspectives

The validation results demonstrate the effectiveness of a posteriori bias correction as a strategy for improving the skill of global hindcast products, particularly in the upper tail of the wave-height distribution where systematic errors are most consequential for hazard applications. Both wave heights and storm surges from the dataset show strong performance across the majority of the validation network, with the high skills concentrated in well-observed extratropical regions characterised by strong synoptic forcing, while larger uncertainties persist in tropical and equatorial areas.

Despite the generally strong global performance, localised biases remain evident in parts of East Asia, western Australia, and, prior to the ad hoc regional adjustment, the Mediterranean Sea. These regions may represent environments where satellite altimetry does not provide a fully reliable reference for bias correction. In the Mediterranean, factors such as the semi-enclosed geometry, short fetch, or the prevalence of young wind-driven seas with steep spectra might affect altimeter retrieval and introduce systematic offsets relative to in situ buoy observations. In East Asia and western Australia, the complex swell climate and the prevalence of mixed sea states could similarly contribute to inconsistencies between altimeter-derived and buoy-measured wave heights. However, the precise causes remain uncertain, and other factors, including closeness of the buoys to the shore, unresolved coastal processes, or regional characteristics of the local atmospheric forcing, cannot be excluded. In all three cases, the residual biases might reflect regional limitations of the reference observational products, rather than deficiencies in the underlying hydrodynamic model or the bias-correction methodology itself. This interpretation is consistent with known regional differences between altimeter and buoy observations reported in the literature (Dodet et al., 2020; Ribal and Young, 2019), and highlights a fundamental challenge in satellite-based bias correction: the correction can only be as accurate as the observational reference on which it relies. Where altimeter biases are present, they will be propagated into the corrected dataset. The Mediterranean regional adjustment described in Sect. 2.2.3 represents a pragmatic response to this limitation, using the denser buoy network available in that enclosed basin to detect and correct the residual offset introduced by the satellite-based procedure.

Several sources of uncertainty should be considered when interpreting and applying the dataset. The bias-correction procedure assumes that model biases are stationary in time, such that correction factors derived from the satellite-observation period (2002–2020) remain applicable to the full hindcast period (1950–2023). The generally consistent performance against

https://doi.org/10.5194/essd-2026-598
Preprint. Discussion started: 18 August 2026

buoy observations spanning multiple decades suggests that the dominant sources of bias remain relatively stable. However, some temporal variability cannot be fully excluded, particularly in regions influenced by long-term climate variability. Additional uncertainty may arise from the evolution of the satellite observing system itself, including differences among altimeter missions, sensor characteristics, retracking algorithms, and changes in spatial sampling through time. Although the altimetry-based wave product from Copernicus Marine Service provides a harmonised multi-mission dataset, residual inter-mission inconsistencies may contribute to uncertainties in the derived correction factors and their temporal transferability (Jiang and Su, 2025; Jiang, 2023).

For storm surges, the absence of a globally consistent observational product equivalent to satellite altimetry introduces an additional challenge. Unlike wave heights, storm surges cannot be directly observed from altimetry: satellite SSH integrates tidal, steric, mesoscale, and surge signals simultaneously, usually separated in the available products using models. This makes it impractical to isolate the surge component at the global scale without substantial additional processing and introducing further uncertainty. Consequently, a direct bias-correction framework analogous to that applied for wave heights cannot be easily applied to storm surges. An alternative and potentially more robust strategy consists of correcting the atmospheric wind forcing rather than the model output directly, as biases in ERA5 wind speeds, particularly under extreme conditions, are a primary driver of surge bias (e.g., Gaffet et al., 2025; Zribi et al., 2026). Such wind-forcing bias correction approaches have shown promise in regional applications and could represent a viable path toward improved global surge datasets. In the interim, the spatial patterns identified in the surge validation suggest that coastal bias-correction layers derived from tide-gauge observations, transferred between coastlines where dataset from surges exhibit similar latitude-dependent and basin-dependent performance characteristics, could provide a practical improvement in nearshore surge estimates.

The underlying hydrodynamic model used for storm surge is based on a barotropic framework. While this approach is computationally efficient and suitable for global applications, it may not fully represent baroclinic processes, equatorial circulation, and other three-dimensional dynamics that influence water levels, particularly in tropical and equatorial regions where lower surge correlations and predominantly negative NBI_{95} values were observed. Although the cyclone-event analyses demonstrate that the dataset reproduces many observed peak water levels and wave conditions, surge representation during intense tropical cyclones could potentially be improved through dedicated high-resolution cyclone modelling or hybrid approaches.

The spatial distribution of observations remains uneven. Wave-buoy and GESLA3 tide-gauge coverage are concentrated primarily along the North American and North European coasts, while observational coverage is substantially lower across much of the Southern Hemisphere, including large parts of South America, Africa, the Indian Ocean, and several tropical regions. Consequently, some regions where model performance is lower are also among the least densely represented in the validation datasets. A denser observational network in tropical and Southern Hemisphere regions would facilitate more robust validation of both wave and storm-surge datasets.

Several of the limitations discussed above can be addressed through regional downscaling approaches that explicitly represent local coastal processes, bathymetry, and shoreline characteristics. The dataset is distributed on a native unstructured

https://doi.org/10.5194/essd-2026-598
Preprint. Discussion started: 18 August 2026

global mesh, which provides a natural interface for regional refinement without interpolation onto regular grids, a methodological advantage that facilitates seamless coupling between global and local modelling frameworks. The availability of corrected wave heights together with spectral wave parameters and peaks provides an opportunity to derive long-term global estimates of wave setup along coastlines. Recent global coastal-characteristics datasets provide nearshore and beach-face slope information at high spatial resolution (Athanasiou et al., 2024), which could be combined with the present wave dataset using empirical formulations (Stockdon et al., 2006) or data-driven techniques to estimate wave setup globally. In regions where the validation metrics are already strong, the dataset can be used to assess the effectiveness of coastal resilience measures and nature-based protection systems, following approaches such as that of Lopes et al. (2026). The simultaneous availability of wave heights, storm surges, and spectral wave parameters spanning 1950–2023, combined with demonstrated performance during cyclone-associated extremes, further enables multivariate and compound-extreme analyses supporting investigations of joint coastal hazards and their associated return periods (Bahmanpour et al., 2026). Together, these capabilities position the dataset as a consistent global baseline for the next generation of coastal hazard assessments, from total water level estimation to compound-event mapping and data-driven emulation of ocean extremes.

Data availability

The global bias-corrected wave-height and filtered storm-surge dataset described in this article is available from the European Commission (EC) Joint Research Centre (JRC) data catalogue at https://doi.org/10.2905/JRC.W0YPDCR (Wadalkar et al., 2026).

Author contributions

ASW conducted the conceptualization, data curation, formal analysis, investigation, methodology, software, validation, visualisation and manuscript drafting. LM guided the supervision, conceptualization, data curation, formal analysis, investigation, methodology, software, validation, visualisation and manuscript drafting. VS supported with data curation, formal analysis, software, validation and visualisation. manuscript review, and revision. MIV, MT, EV, SC, IF and GC contributed with the manuscript review and revision.

Competing interests

The authors declare that they have no conflict of interest.

Financial support

ASW acknowledges support through a PhD scholarship funded by the Italian National Recovery and Resilience Plan (PNRR).

https://doi.org/10.5194/essd-2026-598
Preprint. Discussion started: 18 August 2026

Open Access Earth System Science Data Discussions

References

Alday, M., Accensi, M., Ardhuin, F., and Dodet, G.: A global wave parameter database for geophysical applications. Part 3: Improved forcing and spectral resolution, Ocean Model., 166, 101848, https://doi.org/10.1016/j.ocemod.2021.101848, 2021.

Aleksandrova, N., Veenstra, J., and Muis, S.: Global dataset of storm surges and extreme sea levels for 1950–2024 based on the ERA5 climate reanalysis, Earth Syst. Sci. Data Discuss. [preprint], https://doi.org/10.5194/essd-2025-471, in review, 2025.

Athanasiou, P., van Dongeren, A., Pronk, M., Giardino, A., Vousdoukas, M., and Ranasinghe, R.: Global Coastal Characteristics (GCC): a global dataset of geophysical, hydrodynamic, and socioeconomic coastal indicators, Earth Syst. Sci. Data, 16, 3433–3452, https://doi.org/10.5194/essd-16-3433-2024, 2024.

Bahmanpour, M. H., Tilloy, A., Vousdoukas, M., Federico, I., Coppini, G., Feyen, L., and Mentaschi, L.: Transformed-stationary EVA 2.0: a generalized framework for non-stationary multivariate extremes analysis, Hydrol. Earth Syst. Sci., 30, 2301–2314, https://doi.org/10.5194/hess-30-2301-2026, 2026.

Bakhtyar, R., Maitaria, K., Velissariou, P., Trimble, B., Mashriqui, H., Moghimi, S., Abdolali, A., van der Westhuysen, A. J., Ma, Z., Clark, E. P., and Flowers, T.: A new 1D/2D coupled modeling approach for a riverine-estuarine system under storm events: Application to Delaware River Basin, J. Geophys. Res.-Oceans, 125, e2019JC015822, https://doi.org/10.1029/2019JC015822, 2020.

Barbot, S., Pineau-Guillou, L., and Delouis, J.-M.: Extreme storm surge events and associated dynamics in the North Atlantic, J. Geophys. Res.-Oceans, 129, e2023JC020772, https://doi.org/10.1029/2023JC020772, 2024.

Bernier, N. B., Hemer, M., Mori, N., Appendini, C. M., Breivik, O., de Camargo, R., Casas-Prat, M., Duong, T. M., Haigh, I. D., Howard, T., Hernaman, V., Huizy, O., Irish, J. L., Kirezci, E., Kohno, N., Lee, J.-W., McInnes, K. L., Meyer, E. M. I., Marcos, M., Marsooli, R., Martin Oliva, A., Menéndez, M., Moghimi, S., Muis, S., Polton, J. A., Pringle, W. J., Ranasinghe, R., Saillour, T., Smith, G., Tadesse, M. G., Swail, V., Shimura, T., Voukouvalas, E., Wahl, T., Wang, P., Weisse, R., Westerink, J. J., Young, I. R., and Zhang, Y. J.: Storm surges and extreme sea levels: Review, establishment of model intercomparison and coordination of surge climate projection efforts (SurgeMIP), Weather Clim. Extremes, 45, 100689, https://doi.org/10.1016/j.wace.2024.100689, 2024.

Bessonova, V., Tapoglou, E., Dorrell, R., Dethlefs, N., and York, K.: Global evaluation of wave data reanalysis: Comparison of the ERA5 dataset to buoy observations, Appl. Ocean Res., 157, 104490, https://doi.org/10.1016/j.apor.2025.104490, 2025.

Campos, R. M., Gramcianinov, C. B., de Camargo, R., and da Silva Dias, P. L.: Assessment and calibration of ERA5 severe winds in the Atlantic Ocean using satellite data, Remote Sens., 14, 4918, https://doi.org/10.3390/rs14194918, 2022.

Campos-Caba, R., Alessandri, J., Camus, P., Mazzino, A., Ferrari, F., Federico, I., Vousdoukas, M., Tondello, M., and Mentaschi, L.: Assessing storm surge model performance: what error indicators can measure the model's skill?, Ocean Sci., 20, 1513–1526, https://doi.org/10.5194/os-20-1513-2024, 2024.

Dodet, G., Piolle, J.-F., Quilfen, Y., Abdalla, S., Accensi, M., Ardhuin, F., Ash, E., Bidlot, J.-R., Gommenginger, C., Marechal, G., Passaro, M., Quartly, G., Stopa, J., Timmermans, B., Young, I., Cipollini, P., and Donlon, C.: The Sea State CCI dataset v1: towards a sea state climate data record based on satellite observations, Earth Syst. Sci. Data, 12, 1929–1951, https://doi.org/10.5194/essd-12-1929-2020, 2020.

Dong, X., Liu, Q., Zieger, S., Young, I. R., Li, R., Meucci, A., Sun, J., Wu, K., and Babanin, A. V.: A 45-year high-resolution unstructured wave hindcast for the Australian coast: Validation and climatological insights, Coastal Eng., 204, 104892, https://doi.org/10.1016/j.coastaleng.2025.104892, 2026.

https://doi.org/10.5194/essd-2026-598
Preprint. Discussion started: 18 August 2026

E.U. Copernicus Marine Service Information (CMEMS): Global Ocean L3 Significant Wave Height From Reprocessed Satellite Measurements, Marine Data Store (MDS) [data set], https://doi.org/10.48670/moi-00176, 2021.

Forzieri, G., Feyen, L., Russo, S., Vousdoukas, M., Alfieri, L., Outten, S., Migliavacca, M., Bianchi, A., Rojas, R., and Cid, A.: Multi-hazard assessment in Europe under climate change, Clim. Change, 137, 105–119, https://doi.org/10.1007/s10584-016-1661-x, 2016.

Gaffet, A., Bertin, X., Sous, D., Michaud, H., Roland, A., and Cordier, E.: A new global high-resolution wave model for the tropical ocean using WAVEWATCH III version 7.14, Geosci. Model Dev., 18, 1929–1946, https://doi.org/10.5194/gmd-18-1929-2025, 2025.

Haigh, I. D., Marcos, M., Talke, S. A., Woodworth, P. L., Hunter, J. R., Hague, B. S., Arns, A., Bradshaw, E., and Thompson, P.: GESLA Version 3: A major update to the global higher-frequency sea-level dataset, Geosci. Data J., 10, 293–314, https://doi.org/10.1002/gdj3.174, 2023.

Jiang, H.: Random, Environmental, and Representativeness Errors in Ocean Remote Sensing Versus In Situ Data: An Example of Wave Heights From Altimeters, IEEE Trans. Geosci. Remote Sens., 61, 1–13, https://doi.org/10.1109/TGRS.2023.3285348, 2023.

Jiang, H. and Su, H.: A global gridded dataset of significant wave height via fusion of multi-mission altimetry and numerical hindcast, Earth Syst. Sci. Data Discuss. [preprint], https://doi.org/10.5194/essd-2025-694, in review, 2025.

Jevrejeva, S., Williams, K., Vousdoukas, M. I., and Jackson, L. P.: Future sea level rise dominates changes in worst case extreme sea levels along the global coastline by 2100, Environ. Res. Lett., 18, 024037, https://doi.org/10.1088/1748-9326/acb504, 2023.

Kirezci, E., Young, I. R., Ranasinghe, R., Muis, S., Nicholls, R. J., Lincke, D., and Hinkel, J.: Projections of global-scale extreme sea levels and resulting episodic coastal flooding over the 21st Century, Sci. Rep., 10, 11629, https://doi.org/10.1038/s41598-020-67736-6, 2020.

Kirezci, E., Young, I., Ranasinghe, R., Chen, Y., Zhang, Y., and Rajabifard, A.: Global Dataset of Extreme Sea Levels and Coastal Flood Impacts over the 21st Century, Data, 10, 15, https://doi.org/10.3390/data10020015, 2025.

Koks, E. E., Rozenberg, J., Zorn, C., Tariverdi, M., Vousdoukas, M., Fraser, S. A., Hall, J. W., and Hallegatte, S.: A global multi-hazard risk analysis of road and railway infrastructure assets, Nat. Commun., 10, 2677, https://doi.org/10.1038/s41467-019-10442-3, 2019.

Liu, S., Raghavan, S. V., Nguyen, N. S., Ona, B. J., Ngai, S. T., and Zhang, X.: Improving the regional precipitation simulation corrected by satellite observation using quantile mapping, Remote Sens., 17, 1716, https://doi.org/10.3390/rs17101716, 2025.

Lopes, I. D. R., Federico, I., Vousdoukas, M., Perini, L., Causio, S., Coppini, G., Milella, M., Pinardi, N., and Mentaschi, L.: Numerical modelling framework for assessing dune effectiveness against coastal inundation, Nat. Hazards Earth Syst. Sci., 26, 811–825, https://doi.org/10.5194/nhess-26-811-2026, 2026.

Luo, Y., Wang, D., Gamage, T. P., Zhou, F., Widanage, C. M., and Liu, T.: Wind and wave dataset for Matara, Sri Lanka, Earth Syst. Sci. Data, 10, 131–138, https://doi.org/10.5194/essd-10-131-2018, 2018.

Mentaschi, L., Vousdoukas, M. I., Voukouvalas, E., Sartini, L., Feyen, L., Besio, G., and Alfieri, L.: The transformed-stationary approach: a generic and simplified methodology for non-stationary extreme value analysis, Hydrol. Earth Syst. Sci., 20, 3527–3547, https://doi.org/10.5194/hess-20-3527-2016, 2016.

https://doi.org/10.5194/essd-2026-598
Preprint. Discussion started: 18 August 2026

Mentaschi, L., Vousdoukas, M. I., Voukouvalas, E., Dosio, A., and Feyen, L.: Global changes of extreme coastal wave energy fluxes triggered by intensified teleconnection patterns, Geophys. Res. Lett., 44, 2416–2426, https://doi.org/10.1002/2016GL072488, 2017.

Mentaschi, L., Vousdoukas, M. I., García-Sánchez, G., Fernández-Montblanc, T., Roland, A., Voukouvalas, E., Federico, I., Abdolali, A., Zhang, Y. J., and Feyen, L.: A global unstructured, coupled, high-resolution hindcast of waves and storm surge, Front. Mar. Sci., 10, 1233679, https://doi.org/10.3389/fmars.2023.1233679, 2023.

Moghimi, S., van der Westhuysen, A., Abdolali, A., Myers, E., Vinogradov, S., Ma, Z., Liu, F., Mehra, A., and Kurkowski, N.: Development of an ESMF based flexible coupling application of ADCIRC and WAVEWATCH III for high fidelity coastal inundation studies, J. Mar. Sci. Eng., 8, 308, https://doi.org/10.3390/jmse8050308, 2020.

Muis, S., Irazoqui Apecechea, M., Dullaart, J., de Lima Rego, J., Madsen, K. S., Su, J., Yan, K., and Verlaan, M.: A High-Resolution Global Dataset of Extreme Sea Levels, Tides, and Storm Surges, Including Future Projections, Front. Mar. Sci., 7, 263, https://doi.org/10.3389/fmars.2020.00263, 2020.

Nawarat, K., Reyns, J., Vousdoukas, M. I., Mulholland, E., van Ginkel, K., Feyen, L., and Ranasinghe, R.: Coastal flood risk to European surface transport infrastructure at different global warming levels, Nat. Clim. Chang., 16, 172–178, https://doi.org/10.1038/s41558-025-02510-y, 2026.

Nicholls, R. J., Lincke, D., Hinkel, J., Brown, S., Vafeidis, A. T., Meyssignac, B., Hanson, S. E., Merkens, J.-L., and Fang, J.: A global analysis of subsidence, relative sea-level change and coastal flood exposure, Nat. Clim. Chang., 11, 338–342, https://doi.org/10.1038/s41558-021-00993-z, 2021.

Park, K., Federico, I., Di Lorenzo, E., Ezer, T., Cobb, K. M., Pinardi, N., and Coppini, G.: The contribution of hurricane remote ocean forcing to storm surge along the Southeastern U.S. coast, Coast. Eng., 173, 104098, https://doi.org/10.1016/j.coastaleng.2022.104098, 2022

Piollé, J.-F., Dodet, G., and Quilfen, Y.: ESA Sea State Climate Change Initiative (Sea_State_cci): Global remote sensing daily merged multi-mission along-track significant wave height, L3 product, version 1.1, Centre for Environmental Data Analysis [data set], https://doi.org/10.5285/3ef6a5a66e9947d39b356251909dc12b, 2020.

Ribal, A. and Young, I. R.: 33 years of globally calibrated wave height and wind speed data based on altimeter observations, Sci. Data, 6, 77, https://doi.org/10.1038/s41597-019-0083-9, 2019.

Stockdon, H. F., Holman, R. A., Howd, P. A., and Sallenger, A. H.: Empirical parameterization of setup, swash, and runup, Coast. Eng., 53, 573–588, https://doi.org/10.1016/j.coastaleng.2005.12.005, 2006.

Storlazzi, C. D., Gingerich, S. B., van Dongeren, A., Cheriton, O. M., Swarzenski, P. W., Quataert, E., Voss, C. I., Field, D. W., Annamalai, H., Piniak, G. A., and McCall, R.: Most atolls will be uninhabitable by the mid-21st century because of sea-level rise exacerbating wave-driven flooding, Sci. Adv., 4, eaap9741, https://doi.org/10.1126/sciadv.aap9741, 2018.

Tamizi, A. and Young, I. R.: A dataset of global tropical cyclone wind and surface wave measurements from buoy and satellite platforms, Sci. Data, 11, 106, https://doi.org/10.1038/s41597-024-02955-4, 2024.

Toimil, A., Camus, P., Losada, I. J., Le Cozannet, G., Nicholls, R. J., Idier, D., and Maspataud, A.: Climate change-driven coastal erosion modelling in temperate sandy beaches: Methods and uncertainty treatment, Earth-Sci. Rev., 202, 103110, https://doi.org/10.1016/j.earscirev.2020.103110, 2020.

https://doi.org/10.5194/essd-2026-598
Preprint. Discussion started: 18 August 2026

Vousdoukas, M. I., Mentaschi, L., Voukouvalas, E., Verlaan, M., Jevrejeva, S., Jackson, L. P., and Feyen, L.: Global probabilistic projections of extreme sea levels show intensification of coastal flood hazard, Nat. Commun., 9, 2360, https://doi.org/10.1038/s41467-018-04692-w, 2018.

Vousdoukas, M. I., Ranasinghe, R., Mentaschi, L., Plomaritis, T. A., Athanasiou, P., Luijendijk, A., and Feyen, L.: Sandy coastlines under threat of erosion, Nat. Clim. Chang., 10, 260–263, https://doi.org/10.1038/s41558-020-0697-0, 2020.

Vousdoukas, M. I., Athanasiou, P., Giardino, A., Mentaschi, L., Stocchino, A., Kopp, R. E., Menéndez, P., Beck, M. W., Ranasinghe, R., and Feyen, L.: Small Island Developing States under threat by rising seas even in a 1.5 °C warming world, Nat. Sustain., 6, 1552–1564, https://doi.org/10.1038/s41893-023-01230-5, 2023.

Wadalkar, A. S., Vousdoukas, M. I., Tondello, M., Sharmar, V., Voukouvalas, E., Salvatore, C., Federico, I., Coppini, G. and Mentaschi, L.: A global dataset of bias-corrected waves and storm surge (1950–2023) with improved extremes for hazard mapping [dataset], https://doi.org/10.2905/JRC.W0YPDCR, 2026.

Wahl, T., Haigh, I. D., Nicholls, R. J., Arns, A., Dangendorf, S., Hinkel, J., and Slangen, A. B. A.: Understanding extreme sea levels for broad-scale coastal impact and adaptation analysis, Nat. Commun., 8, 16075, https://doi.org/10.1038/ncomms16075, 2017.

Wang, P. and Bernier, N. B.: Advancing global hindcast of extreme sea levels: Insights from a 65-year study, Weather Clim. Extrem., 50, 100805, https://doi.org/10.1016/j.wace.2025.100805, 2025.

Watson, P. J. and Lim, H.-S.: Extreme value analysis of tide gauge record at the Port of Busan, South Korea, GeoHazards, 4, 497–514, https://doi.org/10.3390/geohazards4040028, 2023.

Wenzel, T., van Westen, C., Sunil, M., Pantaleoni Reluy, N., Marr, P., Glade, T., and Bell, R.: Towards a practical multi-hazard interrelation classification: implications for assessing their impacts, *Nat. Hazards*, 122, 82, https://doi.org/10.1007/s11069-025-07901-0, 2026.

Woodworth, P. L., Hunter, J. R., Marcos, M., and Hughes, C. W.: Towards reliable global allowances for sea level rise, Glob. Planet. Change, 203, 103522, https://doi.org/10.1016/j.gloplacha.2021.103522, 2021.

Zribi, A., Jullien, S., Dodet, G., Bertin, X., and Herry, N.: Sensitivity of Storm Surge Modeling to the Representation of Atmospheric Forcing: The Case Study of Hurricane Irma, in: Coastal Dynamics 2025, edited by: Coelho, C., Hallin, C., Sancho, F., and Silva, P. A., Coastal Research Library, vol. 42, Springer, Cham, 8–14, https://doi.org/10.1007/978-3-032-15477-4_2, 2026.